20th AIAA Aerodynamic Decelerator Systems Technology Conference
May 4–7, 2009
Seattle, WA

AIAA 2009-2964

Dynamic Simulations of Inflatable Aerodynamic Decelerator Concepts

Scott M. Murman*

NASA Ames Research Center, Moffett Field, CA, USA

Abstract

Viscous, free-oscillation simulations with the Overflow solver predict the dynamic response of inflatable aerodynamic decelerator concepts in the supersonic speed regime. These inflatable decelerators are treated as rigid bodies. A stacked-toroid (70° sphere-cone) and tension-cone configuration are contrasted using conditions typical of free-air ballistic-range testing to develop increments in pitch damping coefficient appropriate for trade studies. Similar increments are computed for the stacked-toroid configuration to account for changes in atmosphere between free-air testing on Earth, and a flight vehicle on Mars. The computed increments in pitch damping coefficient for atmospheric changes do not show consistent trends.

1 Introduction

The Mars Science Laboratory (MSL) is scheduled to launch in 2011. This robotic laboratory weighs over 0.8 metric tons, and aims for a site at +2 km Mars Orbital Laser Altimeter (MOLA) elevation. This combination of mass and elevation (low atmospheric density) presents a practical limit to the Viking-heritage supersonic canopy decelerator designed for MSL[1, 2]. Subsequent Mars missions will require larger masses and high elevation, while concurrently decreasing the uncertainty in the landing ellipse. One potential alternative to parachutes, an inflatable aerodynamic decelerator(IAD), is being evaluated as part of NASA's Program to Advance Inflatable Decelerators for Atmospheric Entry (PAI-DAE). The inflatable concepts examined in this work are targeted to deploy in the supersonic speed regime (i.e. after peak entry heating), and have the potential to increase the drag area of the entry capsule by over an order of magnitude.

*Aerospace Engineer. Scott.M.Murman@nasa.gov

The MSL capsule is designed to enter the Martian atmosphere on a lifting trajectory, using thrusters to control roll, pitch, and yaw through peak heating and peak dynamic pressure. After alignment to a predetermined heading, the parachutes begin deployment near Mach 2. With an IAD, this situation will change, and the resultant staging places greater priority on accurate dynamic stability data. The supersonic IAD concepts presume deployment at higher velocity (Mach 5)[3], potentially after discharging a hypersonic-entry inflatable device. Unlike a traditional controlled descent using thrusters, an IAD deployment will produce both attitude and rate dispersions requiring compensation for control. The inflated configuration is intended to fly through the supersonic phase of the descent trajectory. Up to now this portion of the trajectory has used trailing canopy decelerators, which override any dynamic instability associated with the capsule configuration alone.

Computational Fluid Dynamics (CFD) provides a viable alternative to physical testing in many areas of the preliminary design phase, accelerating and improving the development of novel Mars-entry concepts. Dynamic CFD simulations are used to develop an aerodynamic performance database which includes the effects of both static and dynamic responses. The viability and efficiency of this approach has been demonstrated for several atmospheric-entry configurations[4–6]. Previous computational work for inflatable devices focused on a *stacked-toroid* inflatable concept (cf. Hughes et al. [7]) tested in the Aeroballistic Research Facility (ARF) at Eglin Air Force Base (cf. Fig. 1)[5, 8]. This concept consists of an aeroshell surrounded by a membrane filled with inflatable toroids of increasing diameter. The model is treated as rigid sphere-cone shape to match the ballistic-range test article. The current work extends that study by comparison with a *tension-cone* configuration recently evaluated using static wind-tunnel tests[9, 10]. The tension-cone (also referred to in the literature as a *tension-shell* or *hypercone*) is a tensile membrane having a conical deployed shape, supported along its rim by an inflatable torus. As with the stacked-toroid, the configuration is treated here as rigid to match the test articles. The contrast between the tension cone and the more typical sphere-cone geometry, with its greater wealth of aerodynamic data, provides an engineering increment to the pitch damping for the tension cone.

As with the engineering increment due to configuration changes, CFD simulations provide an efficient method for assessing the incremental changes between aerodynamic data gathered from experiments in air, to the flight article in Martian atmosphere. The available data for these flight dynamic increments for decelerators in Martian atmosphere is limited to the data collected by Brown et al. [11] for an initial MSL configuration. The present work extends the available data by examining the sphere-cone configuration in simulations at supersonic (non-reacting) conditions in Martian atmosphere, and compares these against similar results in air.

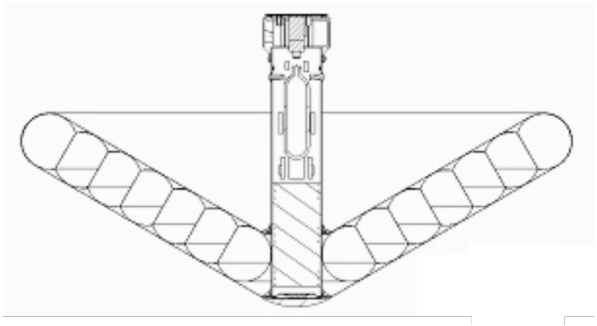

(**a**) Stacked-Toroid

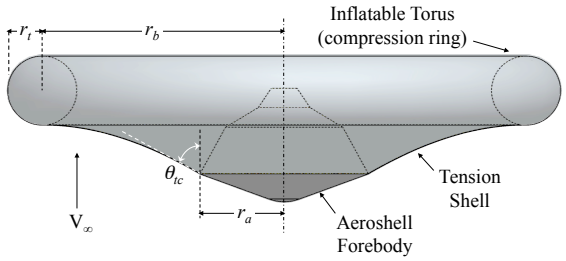

(**b**) Tension-Cone

Figure 1: Inflatable aerodynamic decelerator concepts. Stacked-toroid configuration from Hughes et al. [7] consists of an aeroshell surrounded by a membrane filled with inflatable toroids of increasing diameter. Tension-cone configuration from Clark et al. [9] is a tensile membrane having a conical deployed shape, supported along its rim by an inflatable torus.

2 Decelerator Configurations

The idealized rigid outer mold line (OML) for the inflatable decelerator configurations considered in this work are presented in Fig. 2. These shapes are based upon existing ballistic range and wind tunnel models. The stacked-toroid configuration is one of a parametric series of rigid models tested in the ARF at Eglin Air Force Base[8]. The model is a 70° sphere-cone aeroshell, to match the 70° sphere-cone aeroshell of the tension-cone model, and a cylindrical base section which represents the payload. The tension-cone configuration is based upon the shape developed by Clark et al. [3, 9], using inviscid simulations to ensure an absence of shock interactions on the forebody. The cylindrical aft-body sections for both the stacked-toroid and tension-cone configurations span one-third the maximum diameter of the decelerator, so that for a nominal 5 meter diameter payload the deployed diameter is 15 m. For the tension-cone configuration, this cylindrical aft-body is a truncation of the (idealized) wind tunnel sting assembly.

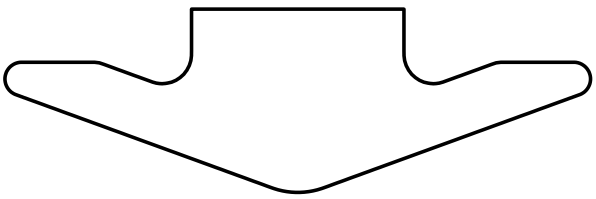

(**a**) Stacked-Toroid

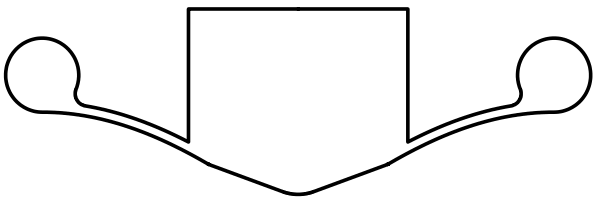

(**b**) Tension-Cone

Figure 2: Outer mold lines for the idealized inflatable aerodynamic decelerator configurations. The center of gravity is located $(0.17D, 0.0, 0.0)$ back from the apex of the sphere-cone.

To provide meaningful dynamic increments, the inertial properties of the models must be treated consistently. As such, the inertial properties of the tension-cone configuration were matched to the ballistic range model for the stacked-toroid configuration. The ballistic-range stacked-toroid model is a homoge-

neous model machined from a tungsten alloy. The tension cone configuration is also treated as an isotropic body of tungsten, with the location of the center of mass (relative to the aeroshell apex) forced to coincide with the center of mass of the stacked toroid configuration.

3 Numerical Approach

The current work utilizes free-oscillation simulations where the vehicle is "pinned" through the center of mass, and only allowed to rotate in the pitch plane in response to the aerodynamic torque. This leverages the inertia of the body to filter the nonlinear response of the wake[4], and provides an accurate model of the dynamic response. In this method, the computational mesh is fixed, and the entire domain rotates with the body. These simulations are performed using the Overflow RANS solver[12] with the Spalart-Allmaras Detached-Eddy Simulation (DES) turbulence model[13]. The DES model includes the low-Reynolds-number corrections for wake flows[14]. Details on the method of performing spatial and temporal resolution studies for these simulations is provided in [5], as well as the typical computational expense.

To reduce the dynamic pitching moment variation from a free-oscillation simulation to standard aerodynamic coefficients we have two independent parameters: the angle of attack and pitch rate (α and q).* Using a linear expansion in both of these variables provides a linear (constant coefficient) aerodynamic model for the pitching moment,

$$\hat{C}_m\left(\alpha, q\right) = C_{m_\circ} + C_{m_\alpha}\Delta\alpha + C_{m_q}\Delta q + e \tag{1}$$

with C_{m_α} referred to as the pitch stiffness, and C_{m_q} the pitch damping (e is a fit error). All of the computed aerodynamic coefficients presented in this work assume the linear aerodynamic model of Eqns. 1, even though some of the trajectories display a nonlinear response. Common approaches to nonlinear modeling do not adequately represent these responses[5], and the use obfuscates the primary goal of this work. A linear aerodynamic model provides a consistent metric to evaluate the effects of shape and atmospheric changes on the dynamic response, and also provides a standardized initial model for inflatable decelerators for trade studies, *etc.*

The tension-cone geometry in Fig. 1b contains a slope discontinuity, or ridge, where the flexible membrane structure attaches to the 70° sphere-cone aeroshell. While the test articles in this work are rigid, this ridge is still present in the geometric model, and imposes requirements on the spatial grid resolution across the bow shock forward of the vehicle. Figure 3 presents Mach contours from three separate simulations of the sphere-cone geometry at $M_\infty = 3.5$. A bow shock forms ahead of the body, and the

*In a free-oscillation motion, $\dot{\alpha}$ and q are equivalent.

flow separates near the maximum diameter location resulting in an unsteady wake. These simulations use a steady-state iterative scheme, and hence the unsteady wake region is a numerical artifact and not representative of an unsteady simulation. In Fig. 3a, a typical body-fitted grid is used on the forebody. The resolution in this forebody grid increases slowly away from the solid surface and provides adequate resolution of the shock at these supersonic conditions. Figure 3b presents the same approach, with the addition of a small ridge ($r/D < 0.001$) mimicking the membrane/aeroshell junction of the tension-cone configuration. In this simulation the region behind the shock is corrupted by spurious entropy waves and regions of boundary-layer separation. The ridge is a disturbance in the subsonic region behind the shock which generates acoustic waves that reflect off the bow shock. The reflection amplifies the spurious entropy waves which pass through the discrete representation of the curved bow shock as it crosses the cell interfaces, commonly referred to as *staircasing* through the shock. This amplification of the shock staircasing in turn leads to a greater boundary layer disturbance, which leads to stronger acoustic disturbance, with the feedback process eventually culminating in the flowfield of Fig. 3b. The solution to this is the removal of the spurious entropy waves through the bow shock. This is commonly accomplished using refinement and/or alignment of the computational mesh to the shock. Within Overflow, and acknowledging that the configuration must dynamically pitch, this entails creating a refined region ahead of the body to resolve the shock. This approach is shown in Fig. 3c, again with the small ridge present. The spurious physics is removed as the feedback amplification is not initialized. This refined region is created manually from preliminary static simulations for each configuration, flow Mach number, and atmospheric gas. The approach applied to the tension-cone configuration is presented in Fig. 3d. A spherical grid spans the shock region, with a separate grid defining the surface geometry and resolving the boundary layer. The computational mesh densities vary between 10 and 20 million grid points, dependent upon configuration, flow conditions, *etc.*

4 Comparisons with Experimental Data

Pressure coefficients from static, steady-state simulations of the tension-cone configuration are compared against recent wind-tunnel data for a rigid test model in Fig. 4. There is excellent agreement between the simulations and experimental data at all conditions. The pressure signature from the ridge joining the membrane to the aeroshell is evident at $r = \pm 23$ mm. The boundary layer remains attached on the forebody at all conditions (cf. Fig. 3d). The comparisons at $M_\infty = 3.5, \alpha = 20^\circ$ are not as strong as the other conditions, however the experimental pressures at these conditions are curious. The measured stagnation pressure is greater than the pressure rise behind a normal shock at similar conditions.

Testing in the ARF at Eglin Air Force Base of the stacked-toroid configuration examined here pro-

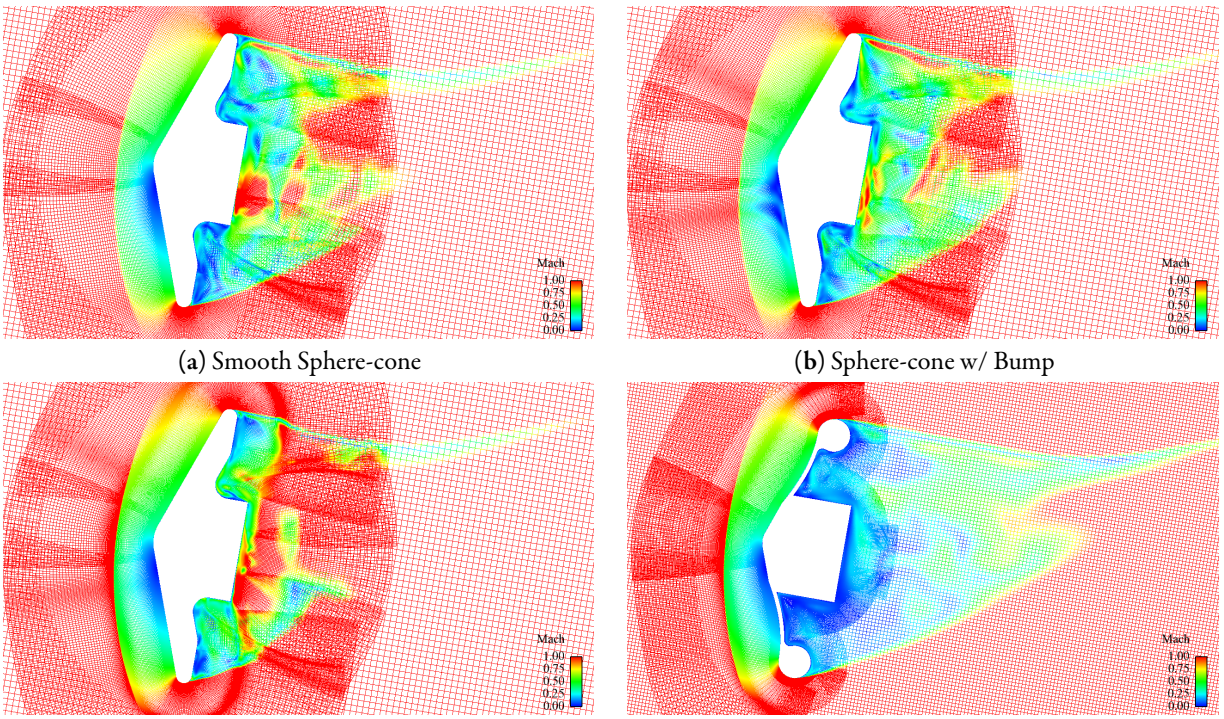

(a) Smooth Sphere-cone (b) Sphere-cone w/ Bump

(c) Shock Refinement w/ Bump (d) Tension-cone

Figure 3: Mach contours ($M \in [0, 1]$) demonstrating the shock resolution requirements in the presence of aeroshell geometric perturbations. ($M_\infty = 3.5, \alpha = 10°, Re_D = 5.7 \text{ x } 10^6$).

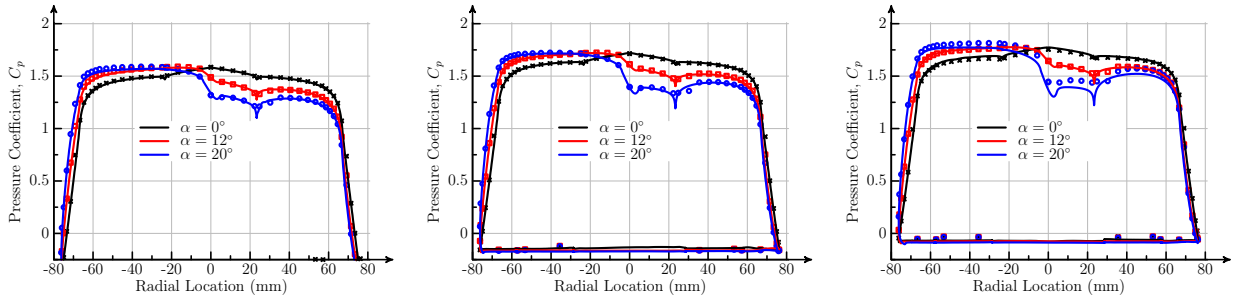

(a) $M_\infty = 1.65$ (b) $M_\infty = 2.5$ (c) $M_\infty = 3.5$

Figure 4: Variation of pressure coefficient in the pitch plane for static, steady-state simulations of the tension-cone configuration in Fig. 2b. Symbols represent measured data from Clark et al. [10]. Windward values have positive coefficient, leeward negative. ($Re_D = 1.0 \text{ x } 10^6$).

duced a single trajectory, which oscillates over roughly $\alpha_t \approx \pm 15°$. The aerodynamic coefficients are reduced from shadowgraph images using the Comprehensive Aerodynamic Data Reduction System for Aeroballistic Ranges (CADRA) software developed by Yates[15]. With a single trajectory, only linear estimates of the aerodynamic coefficients are available from the free-flight testing. These coefficients are compared against a set of free-oscillation simulations at three Mach numbers in the supersonic regime in

Fig. 5, each released at $\alpha = 20°$. The pitch stiffness is in very good agreement, with the differences less than 5%. The pitch damping coefficients are also in good agreement with the available data. The variation of drag coefficient over the complete oscillation is presented against the nominal values from the range testing. The agreement is very good, though the range testing does not provide a model for the dynamic hysteresis which occurs in the drag variation. Assessing the effects of dynamics on the lift and drag variation for atmospheric decelerators requires a revision of current aerodynamic modeling approaches, and is beyond the scope of the current work. The remainder of this article focuses on the pitch stiffness and pitch damping.

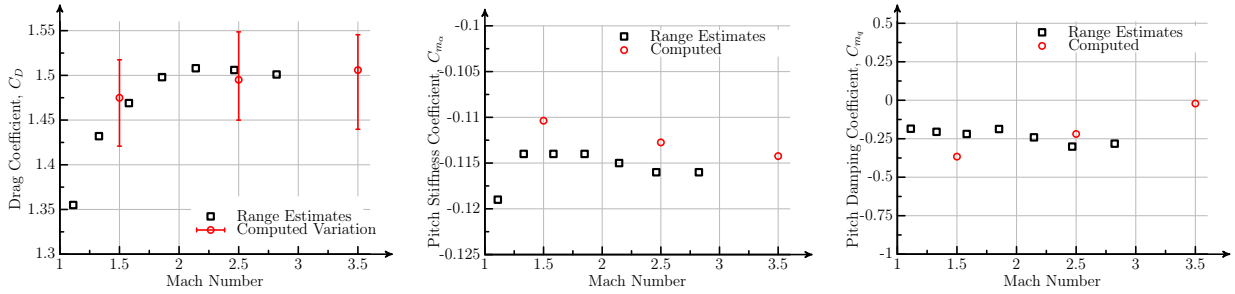

(a) Drag (b) Pitch Stiffness (c) Pitch Damping

Figure 5: Variation of aerodynamic coefficients for the stacked-toroid configuration in Fig. 2a released at $\alpha = 20°$. Symbols represent fit values to a single range trajectory oscillating over $\alpha \approx \pm 15°$ from Yates [8].

5 Shape Changes

Examining the stacked-toroid simulations of Fig. 5 in greater detail, the computed trajectories (observations) and reconstructions assuming a linear aerodynamic model (Eqn. 1) are presented in Fig. 6. Two simulation results are presented: a high-angle-of-attack, high-pitch-rate release, and a low-angle-of-attack, low-pitch-rate release. As noted in [5], typical supersonic decelerator configurations demonstrate a rate-dependent dynamic response. Using a linear aerodynamic model assumption, this leads to two separate estimates for the aerodynamic coefficients for each of the two release conditions. These estimates are presented in Fig. 7 for the stacked-toroid configuration, with a linear regression over the three computed Mach numbers co-plotted. Consistent with the results in [5], the lower angle of attack release demonstrates a greater tendency for instability, and an increase in the nonlinearity in the aerodynamic response. The latter is noted by the discrepancies between the observed and reconstructed trajectories. The $\alpha = 5°$ trajectory at $M_\infty = 2.5$ presents a limit cycle, where the decelerator alternates between increasing and decreasing in pitch amplitude and rate.

The nonlinear response at the lower angle of attack releases leads to an increase in the estimated pitch

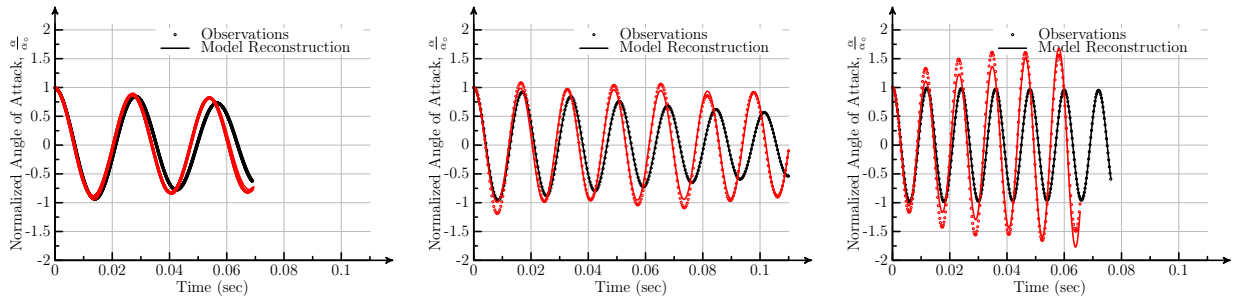

(a) $M_\infty = 1.5$ (b) $M_\infty = 2.5$ (c) $M_\infty = 3.5$

Figure 6: Computed and reconstructed trajectories for the stacked-toroid configuration. $\alpha = 5°$ releases are in red, with $\alpha = 20°$ releases in black.

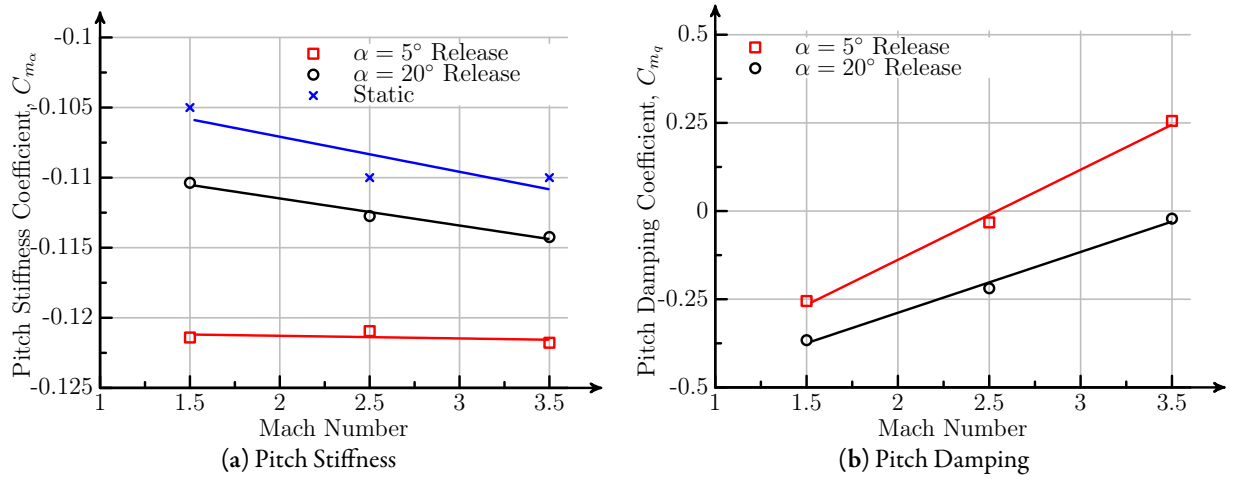

(a) Pitch Stiffness (b) Pitch Damping

Figure 7: Variation of aerodynamic coefficients for the stacked-toroid configuration assuming a linear aerodynamic model. Lines are linear regressions through the data points.

stiffness, which is also evident in the increase in oscillation frequency. The linear pitch stiffness computed from static simulations is included for comparison. The results of the static simulations are in better agreement with the high-angle-of-attack release data, which is consistent with the observed linear response for these dynamic simulations. While the increase in pitch stiffness for the $\alpha = 5°$ release data is in part due to the assumption of linear aerodynamics to model a nonlinear response, the effect cannot be ignored. If the design envelope prescribes small oscillations, and a linear aerodynamic model is assumed, then the dynamic response indicates an increase in pitch stiffness coefficient is necessary. Further, linear aerodynamic data based upon static CFD simulations or wind tunnel data does not accurately capture the nonlinear coupled response of the dynamic vehicle.

Computed and reconstructed trajectory data for free-oscillation simulations of the tension-cone configuration at supersonic conditions are presented in Fig. 8. Comparisons of the reduced aerodynamic data against the computed results for the stacked-toroid configuration are presented in Fig. 9. In general, the

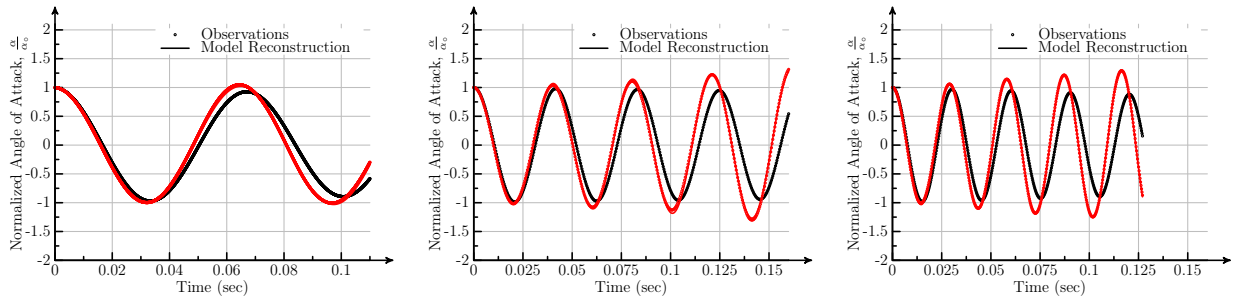

(a) $M_\infty = 1.5$ (b) $M_\infty = 2.5$ (c) $M_\infty = 3.5$

Figure 8: Computed and reconstructed trajectories for the tension-cone configuration. $\alpha = 5°$ releases are in red, with $\alpha = 20°$ releases in black.

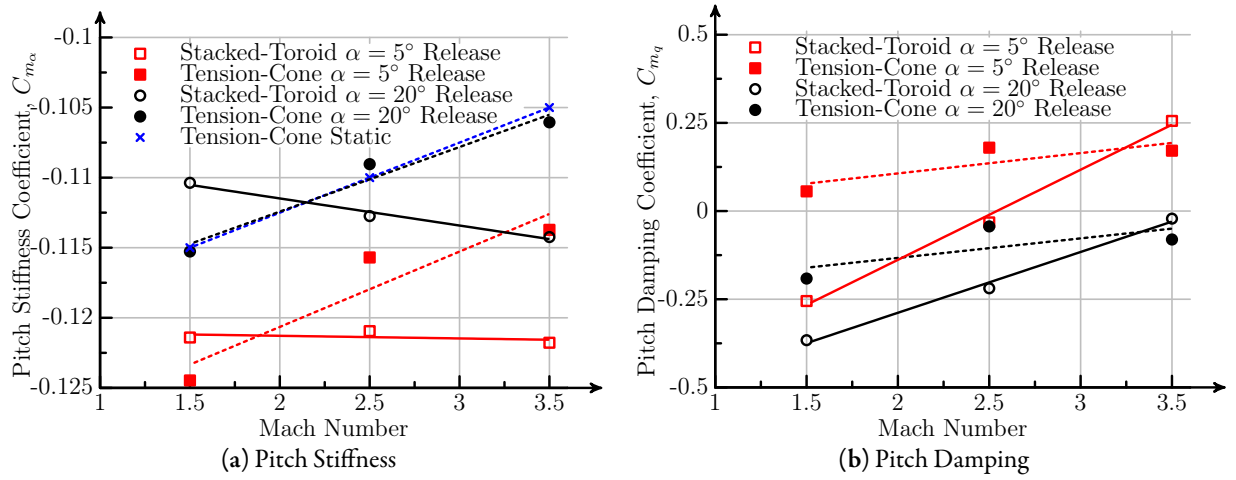

(a) Pitch Stiffness (b) Pitch Damping

Figure 9: Variation of aerodynamic coefficients for the stacked-toroid and tension-cone configurations assuming a linear aerodynamic model. Lines are linear regressions through the data points.

lower-oscillation tension-cone simulations are slightly less stable than the sphere-cone configuration at the lower speeds, though the trajectory data at Mach 1.5 is limited. The data is consistent with a tension-cone limit-cycle at a greater amplitude than the sphere-cone. The pitch stiffness decreases with increasing Mach number, opposite the trend of the sphere-cone. The pitch stiffness coefficient estimated from static simulations is included for comparison, and as with the stacked-toroid configuration this data is in good agreement with the (linear response) higher-angle-of-attack release data. Unlike the static computations of the tension-cone configuration presented in Fig. 4, in the dynamic simulations the boundary layer does separate at the ridge joining the aeroshell and membrane in the larger oscillation simulations. This occurs when the pitch oscillation changes direction, as the inertia of the fluid lags the response, forcing the boundary layer to separate. As the pitch oscillation continues, the boundary layer eventually reattaches. Figure 10 presents Mach contours in the pitch plane for the $M_\infty = 3.5$ simulation released at $\alpha = 20°$. The angle of attack is nominally the same in both images, with the body pitching up in Fig. 10a, and pitch-

ing down in the sister image. As the body rotates back towards the trim point, the boundary layer must reverse direction, forcing a separation from the ridge joining the aeroshell and membrane. The lower pitch rate for the low-amplitude oscillation reduces the inertia difference between the body and fluid, and in the current $\alpha = 5°$ releases separation does not occur.

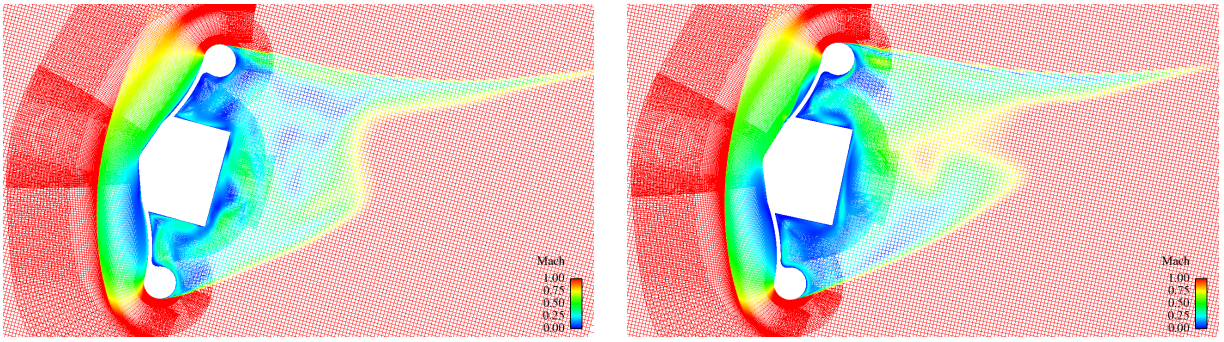

(a) Pitch Up **(b)** Pitch Down

Figure 10: Mach contours ($M \in [0, 1]$) in the pitch plane showing boundary layer separation from the junction of the aeroshell and membrane when the pitch oscillation reverses direction. ($M_\infty = 3.5$, $\alpha \approx 13.6°$, $Re_D = 5.7 \text{ x } 10^6$)

6 Atmosphere Changes

The effect of atmospheric gas on the dynamics is examined using the stacked-toroid configuration. Previous (preliminary) experimental results from aero-ballistic range tests at NASA Ames for a lifting MSL configuration indicate that moving from air to CO_2, at similar atmospheric density, can change the dynamic response (cf. Fig. 11 and Brown et al. [11]). In the current work, the atmosphere is treated as a perfect gas, using nominal values of $\gamma = 1.29$, $Pr = 0.66$, and modifying Sutherland's law for the molecular viscosity. The atmospheric density and temperature are assumed the same as the free-air range testing used as a baseline from Sec. 5. The Reynolds number for the current simulations is roughly one order of magnitude greater than the Reynolds number in the free-flight data of [11] (10^6 *vs.* 10^5). As the model density (virtual and range) matches tungsten alloy, this results in a dynamic similarity (ρ_{model}/ρ_∞) within roughly an

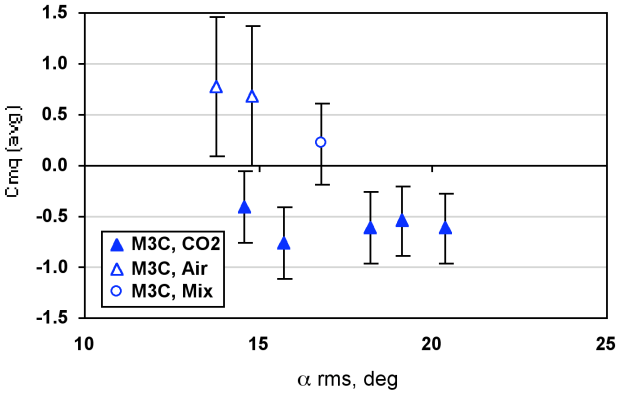

Figure 11: Fig. 16 from Brown et al. [11]. Effect of changing atmospheric gas at constant dynamic similarity for a preliminary MSL configuration. Reproduced with permission.

order of magnitude (low) of a flight vehicle on Mars*.

Mach contours in the pitch plane for simulations in air and Martian atmosphere passing through the trim point during dynamic simulations at Mach 3.5 are presented in Fig. 12. The bow shock moves closer to the surface in the simulation in Mars atmosphere, though in general the changes are relatively minor at these non-reacting conditions.

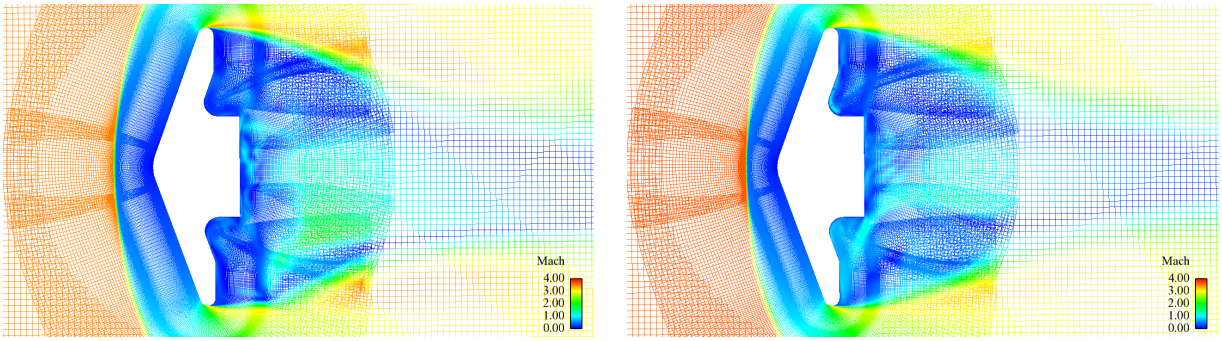

(a) Air **(b)** Mars

Figure 12: Mach contours ($M \in [0, 4]$) in the pitch plane for non-reacting simulations in air and Martian atmosphere. ($M_\infty = 3.5, \alpha \approx 0°, Re_D = 5.7 \text{ x } 10^6$)

Figures 13 and 14 present the oscillation data and reduced aerodynamic coefficients for the stacked-toroid simulations in Mars atmosphere compared against simulations in air. Consistent with the minor changes to the fluid dynamics in Fig. 12, the changes to the aerodynamic parameters are likewise modest, and no significant trends are present. There are several differences between the current simulations, and the range results of Fig. 11, specifically; different configurations, lifting *vs.* non-lifting body, Reynolds number, dynamic similarity, and aerodynamic modeling assumptions. Further work is required to understand the specific drivers which may cause increments between atmospheric conditions in the supersonic regime.

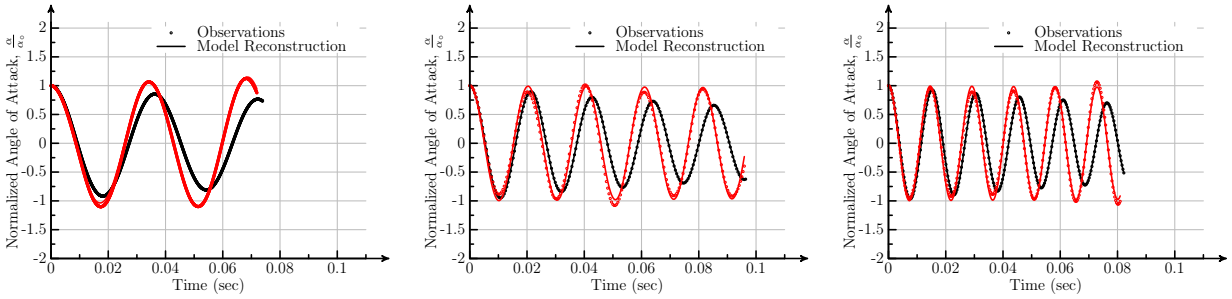

(a) $M_\infty = 1.5$ **(b)** $M_\infty = 2.5$ **(c)** $M_\infty = 3.5$

Figure 13: Computed and reconstructed trajectories for the stacked-toroid configuration in Mars atmosphere with same density as Earth sea-level free-air testing. $\alpha = 5°$ releases are in red, with $\alpha = 20°$ releases in black.

*We assume a vehicle packing density of roughly 200 kg/m^3, and an altitude of 10-20 km.

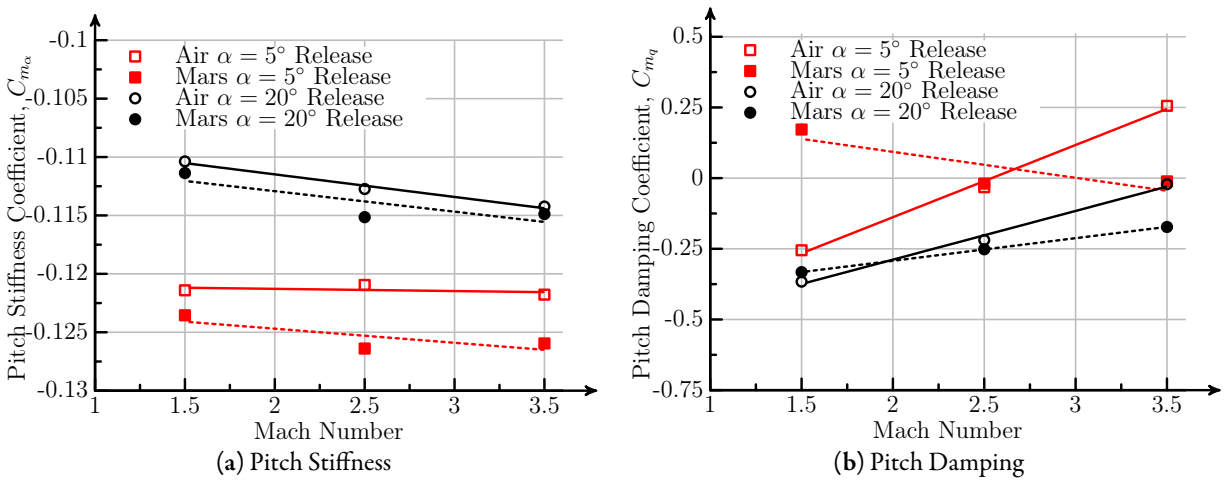

(a) Pitch Stiffness (b) Pitch Damping

Figure 14: Variation of aerodynamic coefficients for the stacked-toroid configuration in Mars atmosphere with same density as Earth sea-level free-air testing. Assumes a linear aerodynamic model. Lines are linear regressions through the data points.

7 Summary

Hybrid-RANS simulations of free-oscillation motion were performed to examine the dynamic pitch response of novel inflatable aerodynamic decelerator concepts for descent through Martian atmosphere. These inflatable concepts were treated as rigid bodies as a first approximation. The focus is on developing meaningful aerodynamic coefficients to represent the response in the supersonic speed regime for use in trade studies and planning of future experimental programs. Two separate increments were calculated: contrasts between a stacked-toroid (70° sphere-cone) and tension-cone concept, and the effect of changes between free-air testing and a flight vehicle in Martian atmosphere.

Following [5] for similar aerodynamic decelerator configurations, the current dynamics demonstrate a (nonlinear) rate-dependent response. In this work, this effect is handled by separately treating the high-amplitude and low-amplitude oscillations using a linear aerodynamic model. This highlights the change in pitch stiffness that occurs for low-amplitude dynamic oscillations due to the nonlinear aerodynamic coupling between the body motion and fluid response. To accurately reproduce the observed trajectory data increases in the linear pitch stiffness coefficient are required over that provided by static simulations or wind tunnel testing.

The tension-cone configuration contains a small but consistent destabilizing increment in pitch damping coefficient at Mach 1.5 and 2.5 over the sphere-cone configuration. Boundary-layer separation occurs at the junction of the aeroshell and membrane of the tension-cone configuration during dynamic high-amplitude oscillations. No separation occurs in similar conditions during static simulations, or the lower-amplitude oscillations.

Non-reacting simulations in Martian atmosphere were contrasted with similar results in free-air for the

stacked-toroid configuration. These computed results demonstrate little effect of changing atmospheric gas, either in the flowfield features or computed aerodynamic coefficients. Previous ballistic range data indicated a consistent increment between testing in CO_2 and air, and further work is required to understand the specific drivers which may cause increments between atmospheric conditions in the supersonic regime.

Acknowledgments

Thanks to Ian Clark of the Georgia Institute of Technology for his invaluable assistance understanding the outer-mold-line and experimental data for the tension-cone configuration.

References

[1] Braun, R.D. and Manning, R.M., "Mars Exploration Entry and Landing Challenges," *Journal of Spacecraft and Rockets*, 44(2):310–323, March 2007.

[2] Christian, J., Wells, G., Lafleur, J., Verges, A., and Braun, R., "Extension of Traditional Entry Descent and Landing Technologies for Human Mars Exploration," *Journal of Spacecraft and Rockets*, 45(1), January 2008.

[3] Clark, I.G., Hutchings, A.L., Tanner, C.L., and Braun, R.D., "Supersonic Inflatable Aerodynamic Decelerators For Use On Future Robotic Missions to Mars," *Journal of Spacecraft and Rockets*, 46(2): 340–352, 2009.

[4] Murman, S.M. and Aftosmis, M.J., "Dynamic Analysis of Atmospheric-Entry Probes and Capsules," AIAA Paper 2007-0074, January 2007.

[5] Murman, S.M., "Dynamic Viscous Simulations of Atmospheric-Entry Capsules," AIAA Paper 2008-6911, August 2008.

[6] Murman, S.M., "Dynamic Simulations of Atmospheric-Entry Capsules," *Journal of Spacecraft and Rockets*, In Print, 2009.

[7] Hughes, S.J., Dillman, R.A., Starr, B.R., Stephan, R.A., Lindell, M.C., Player, C.J., and Cheatwood, F.M., "Inflatable Re-entry Vehicle Experiment (IRVE) Design Overview," AIAA Paper 2005-1636, 2005.

[8] Yates, L.A. and Chapman, G.T., "Analysis of Data from Ballistic Range Tests of PAI-DAE Vehicles," Aerospace Computing, Inc., Report, November 2007.

[9] Clark, I.G., Cruz, J.R., Hughes, M.S., Ware, J., and Madlangbayan, A., "Supersonic Wind Tunnel Tests of a Rigid Tension Cone Inflatable Aerodynamic Decelerator," AIAA Paper 2009-2967, May 2009.

[10] Clark, I.G., Cruz, J.R., Braun, R.D., "Computational Analysis of a Tension Cone Supersonic Inflatable Aerodynamic Decelerator," in *IEEE Aerospace Conference*, March 2009.

[11] Brown, J., Yates, L., Bogdanoff, D., Chapman, G., Loomis, M., and Tam, T., "Free Flight Testing in Support of the Mars Smart Lander Aerodynamics Database," AIAA Paper 2002-4410, August 2002.

[12] Nichols, R.H., Tramel, R.W., and Buning, P.G., "Solver and Turbulence Model Upgrades to OVERFLOW 2 for Unsteady and High-Speed Applications," AIAA Paper 2006-2824, 2006.

[13] Spalart, P. R., "Strategies for Turbulence Modeling and Simulations," *International Journal of Heat and Fluid Flow*, 21:252–363, 2000.

[14] Spalart, P. R., Deck, S., Shur, M.L., Squires, K.D., Strelets, M.Kh., and Travin, A., "A New Version of Detached-Eddy Simulation, Resistant to Ambiquous Grid Densities," *Theoretical Computational Fluid Dynamics*, 20:181–195, 2006.

[15] Yates, L.A., "A Comprehensive Aerodynamic Data Reduction System for Aeroballistic Ranges," Wright Laboratory, Technical Report 96-7059, October 1996.